

# SPATIAL VARIATIONS OF THE SYNCHROTRON SPECTRUM WITHIN TYCHO'S SUPERNOVA REMNANT (3C 10): A SPECTRAL TOMOGRAPHY ANALYSIS OF RADIO OBSERVATIONS AT 20 AND 90 CENTIMETER WAVELENGTHS

D. M. KATZ-STONE

United States Naval Academy, Physics Department 9C Annapolis, MD 21402-5026; dkatz@nadm.navy.mil

N. E. KASSIM

Code 7213, Naval Research Laboratory, Washington, DC 20375-5351; nkassim@shimmer.nrl.navy.mil

T. JOSEPH W. LAZIO<sup>1</sup>

Code 7210, Naval Research Laboratory, Washington, DC 20375-5351; lazio@rsd.nrl.navy.mil

AND

R. O'DONNELL<sup>2</sup>

United States Naval Academy, Annapolis, MD 21402-5026; ode31@earthlink.net

Received 1999 May 25; accepted 1999 September 10

## ABSTRACT

We present subarcminute-resolution ( $\approx 10''$ ), high-dynamic range radio observations of Tycho's supernova remnant (3C 10) at  $\lambda = 20$  cm and  $\lambda = 90$  cm with the Very Large Array (VLA). The thermal-noise-limited 90 cm image has been compensated properly for the noncoplanar characteristics of the VLA and is the most sensitive low-frequency image of this source presently available. We use these images to search for spatial variations in the continuum radio spectral index within the remnant. Such spatial variations should be related to the electron acceleration processes associated with the evolution of the blast wave. We have also utilized, for the first time in an analysis of a supernova remnant, spectral tomography to search for localized regions within which the spectral index is different from the surroundings. We have identified 13 filaments, ranging in size from  $\approx 40''$  to  $\approx 260''$ , embedded in a smoother, background component. The average spectral index of the filaments ( $\langle\alpha\rangle = -0.52 \pm 0.02$ ) is consistent with that of the background component ( $\langle\alpha\rangle = -0.500 \pm 0.007$ ). However, the filaments in the outer rim show a trend such that brighter filaments have a flatter spectral index. This trend may be due to either supernova remnant (SNR) blast wave–ambient medium interactions or internal inhomogeneities of the magnetic field within the remnant. These hypotheses could be tested by an image at comparable resolution and fidelity at a third frequency.

*Subject headings:* acceleration of particles — radiation mechanisms: nonthermal —  
 radio continuum: general — supernova remnants — supernovae: individual (Tycho)

## 1. INTRODUCTION

A new star observed by Tycho Brahe (1573) is now identified as a supernova whose remnant (SNR) is 3C 10 (SN 1572, Tycho SNR, SNR 120.1  $\pm$  1.4; Lozinskaya 1992 and references therein). The explosion itself was mostly likely a Type Ia supernova, and the remnant seems to be moving into the Sedov adiabatic phase of evolution with an average expansion rate of approximately  $0.1\% \text{ yr}^{-1}$  (e.g., Strom et al. 1982; Tan & Gull 1985; Reynoso et al. 1997). The distance to 3C 10 is approximately 3 kpc, placing it on the near side of the Perseus arm (Lozinskaya 1992). At both radio (e.g., Reynoso et al. 1997) and X-ray (e.g., Hwang & Gotthelf 1997) wavelengths, 3C 10 has a limb-brightened shell morphology with a diameter of approximately  $8'$  (7 pc at a distance of 3 kpc), within which the magnetic field is primarily radial.

Supernova remnants are thought to be the primary sites at which Galactic cosmic rays are accelerated, with the acceleration process probably being first- or second-order Fermi acceleration (Jones et al. 1998 and references therein). X-ray and gamma-ray observations of various remnants (e.g., SN 1006 and IC 443) have indeed been able to identify localized regions whose nonthermal spectra are consistent

with ongoing shock acceleration (e.g., Koyama et al. 1995; Keohane et al. 1997; Tanimori et al. 1998). However, X-ray and gamma-ray observations typically have poor angular resolution (greater than  $1'$ ) and low sensitivity, so that only the most efficient regions of particle acceleration can be identified. In contrast, high-resolution, high-dynamic range, multiwavelength radio observations can search for regions of less intense particle acceleration as well as probe for spatial variations within a remnant (e.g., Anderson & Rudnick 1993 for a summary). Changes either in the strength of the acceleration process or between processes can reveal themselves through the slope of the radio spectrum, primarily through the spectral index  $\alpha$  ( $S_\nu \propto \nu^\alpha$ ).

As a nearby and relatively large SNR, 3C 10 offers an excellent laboratory in which to probe for spatial variations in the acceleration process. However, only a few high-resolution, multiwavelength observations of 3C 10 have been conducted, and the results are inconclusive. Klein et al. (1979) found no evidence for significant spatial variation of the spectral index across 3C 10. Duin & Strom (1975) found significant steepening of the spectrum near the center of the source. Roger, Bridle, & Costain (1973) concluded that the spectrum was comprised of two components. Vinyaikin et al. (1987) placed limits on the relative strengths of these components. Table 1 summarizes previous observations.

This paper reports matched, high-resolution  $\lambda = 20$  cm and  $\lambda = 90$  cm observations of 3C 10, from which we deter-

<sup>1</sup> NRL-NRC Research Associate.

<sup>2</sup> Present address: US Navy, Kesseling Atomic Power Laboratory, Scotia, NY 12302.

TABLE 1  
PREVIOUS OBSERVATIONS: INTEGRATED SPECTRA

Frequency Range (GHz)	Spectral Index	Reference
$0.015 < \nu < 0.33$ .....	-0.9	1
$0.33 < \nu$ .....	-0.48	1
$1.4 < \nu < 10.7$ .....	-0.55	2
$0.018 < \nu < 0.5$ .....	-0.95	3
$0.5 < \nu$ .....	-0.35	3
$0.61 < \nu < 1.4$ .....	-0.7 <sup>a</sup>	4
$0.04 < \nu < 10.7$ .....	-0.61	5
$0.013 < \nu < 15$ .....	-0.61	6

<sup>a</sup> This is only for the small-scale features (less than 3') which are mainly in the outer regions; working at 1' resolution, these authors find that the spectral index on large scales is steeper ( $\alpha = -1.0$ ) toward the center.

REFERENCES.—(1) Braude et al. 1970; (2) Kundu & Velusamy 1971; (3) Roger et al. 1973; (4) Duin & Strom 1975; (5) Klein et al. 1979; (6) Vinyaikin et al. 1987.

mine the spatial distribution of the spectral index across the remnant. In § 2 we describe the observations, in § 3 we discuss the determination of the spectral index as a function of position within the remnant, in § 4 we discuss the implications for theories of particle acceleration, and we present our conclusions in § 5.

## 2. OBSERVATIONS

In this section we discuss the observations of 3C 10 as well as the steps we have taken to ensure that the spectral indexes that we calculate are robust. The data analyzed in this paper were obtained from the Very Large Array (VLA). The 20 cm data acquisition and initial analysis were presented by Reynoso et al. (1997). Their observations were at 1375 and 1635 MHz with all four configurations of the VLA during 1994–1995. The 90 cm observations and analysis are new and are discussed below.

Figure 1 shows the total intensity image of 3C 10 at  $\lambda = 20$  cm, smoothed to an effective resolution of  $9''.52 \times 7''.65$  so as to agree with that of the  $\lambda = 90$  cm observations (see below).

### 2.1. $\lambda = 90$ cm

The 90 cm observations are the combination of four observing sessions at the VLA, with the array in three different configurations. Table 2 summarizes these observations. In all observations, dual circular polarization was recorded at a center frequency of approximately 333 MHz with a bandwidth of 2.5 MHz. The total time on source was 2.2 hr. The range of array configurations means that our final image will be sensitive to angular scales from approximately

TABLE 2  
VLA 90 CENTIMETER OBSERVING LOG

Date	VLA Configuration	Time on Source (minutes)
1991 November 24.....	B	16
1992 October 24 .....	A	5.3
1993 March 1 .....	B	22
1993 July 10 .....	C	88

NOTE.—All observations recorded dual circular polarization at a center frequency of 333 MHz with a bandwidth of 2.5 MHz.

8'' (the angular resolution of the A configuration) to approximately 30' (the largest angular scale for the C configuration).

Initial calibration followed standard procedures within the Astronomical Image Processing System (AIPS). The primary flux density calibration was based upon 3C 48, 3C 147, and 3C 286, whose flux densities were taken to be 42.47, 53.65, and 26.34 Jy, respectively. Phase calibration was accomplished with frequent observations of 3C 123 and 3C 380. The visibility data from each observing session were calibrated independently, then combined before beginning the imaging procedure. The hybrid mapping described below incorporated 10–15 passes of self-calibration, both phase-only and phase-and-amplitude.

A conventional two-dimensional inversion of the three-dimensional visibility function, as measured by a non-coplanar (i.e., non-east-west) array like the VLA, introduces phase errors in the image plane that increase with distance from the phase center. The “three-dimensional” problem becomes severe at long wavelengths where the primary beam is large and contains hundreds of discrete sources that must be properly deconvolved to achieve thermal-noise-limited or classical-confusion-limited images.

Cornwell & Perley (1992) developed a polyhedron algorithm in which the three-dimensional “image volume” is approximated by many two-dimensional “facets.” This algorithm and similar ones now exist within commonly used astronomical imaging packages (AIPS and SDE) with their only limitation being their computational expense. The results presented in this paper were generated within the SDE polyhedron imaging algorithm “dragon,” whose code was ported to an SGI Origin 2000 computer available within the Department of Defense High Performance Computing Modernization Program.

We used two iterations of polyhedral faceting to produce our final image. In the first iteration, we imaged the entire primary beam (156' FWHM) at a low resolution ( $\approx 20''$ , comparable to the resolution of the B configuration VLA). We used this low-resolution “finder” image to identify all sources brighter than 20 mJy beam<sup>-1</sup> ( $\approx 6\sigma$ ) in the primary beam. We also identified all sources from the 4C catalog whose primary-beam-attenuated sidelobes were larger than 10 mJy beam<sup>-1</sup> within the field of view. A total of 81 sources, including 3C 10, were identified.

In the second iteration, a small region around each source was imaged at the limiting angular resolution inherent in the visibility data ( $\approx 8''$ ). Restricting the facets to be only slightly larger than a source exploits the fact that the radio sky is mostly dark. It also obviates the pixellation of the entire primary beam at this high resolution, a task that remains computationally intensive.

After this second iteration, all identified sources except 3C 10 were subtracted from the visibility data. The visibilities in this subtracted visibility data set will be dominated by 3C 10, though there will be a contribution from weaker sources we have not identified. Sources not identified have peak brightnesses less than 20 mJy beam<sup>-1</sup>. The majority of the features that we identify within 3C 10 have *mean* brightnesses greater than 20 mJy beam<sup>-1</sup>. Thus, the sidelobes from any weak source are unlikely to corrupt our identification of any features within 3C 10 or measurements we make on them.

Figure 2 shows our final image of 3C 10 that was produced from this subtracted visibility data set. We estimate that

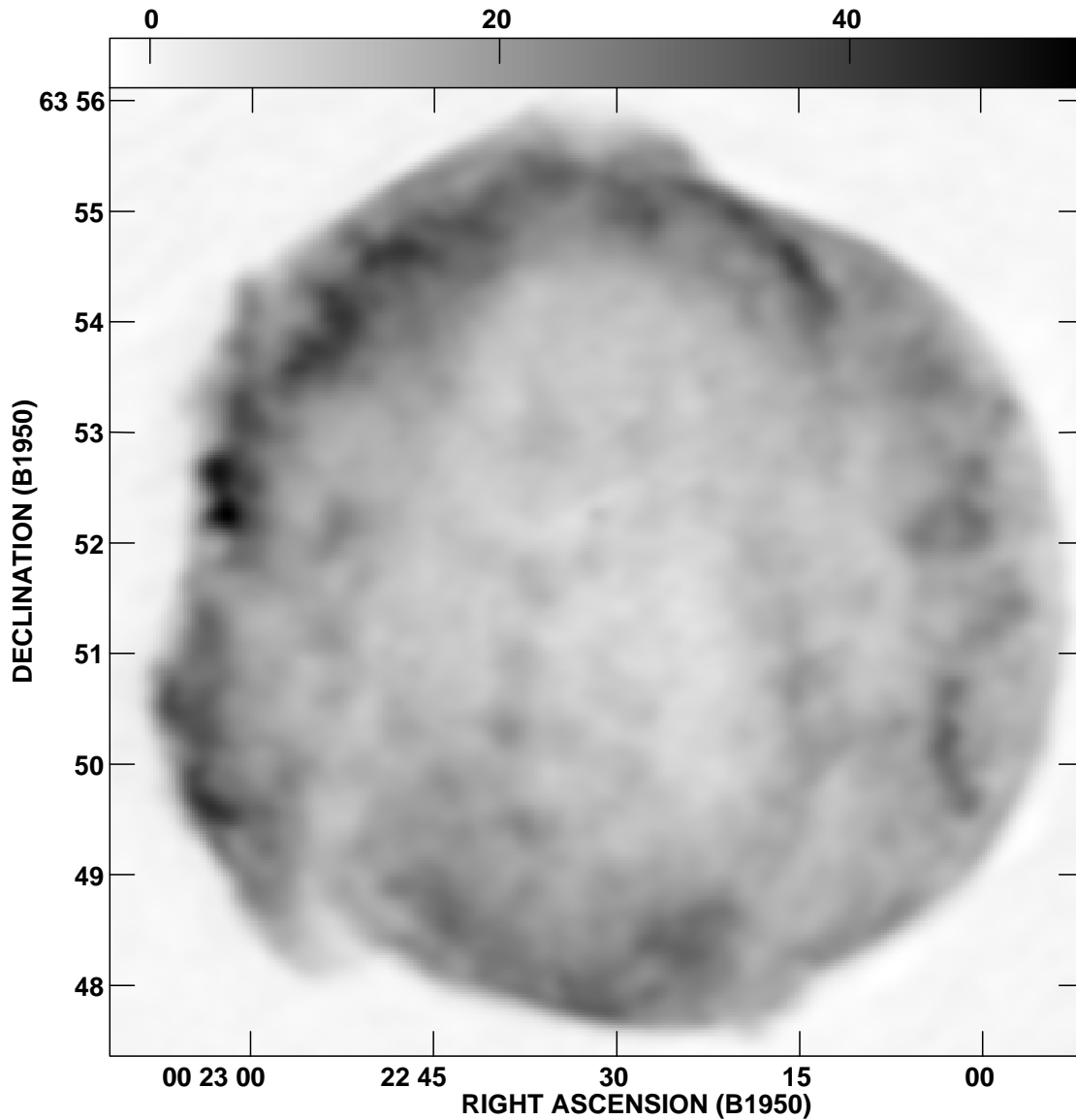


FIG. 1.—3C 10 at 20 cm. This image was produced from data acquired by Reynoso et al. (1997) and smoothed to an effective resolution of  $9''.52 \times 7''.65$ . Gray-scale levels are linear between  $-2.2$  and  $53.3 \text{ mJy beam}^{-1}$ .

the thermal-noise limit in our combined-configuration image is  $0.88 \text{ mJy beam}^{-1}$ ; the actual off-source rms level is  $0.9 \text{ mJy beam}^{-1}$ .

## 2.2. Matching Observations

Because the observations at the two wavelengths of 3C 10 were not conducted simultaneously, we took a number of steps to ensure that the spectral indexes determined are robust.

First, determining accurate spectral indexes requires an accurate determination of the remnant's flux density at both wavelengths. For an interferometer—like the VLA—the flux density measured depends upon the length of the shortest baselines used, i.e., the smallest spatial frequency sampled. Furthermore, the 20 cm data have an intrinsically higher angular resolution than the 90 cm data. In order to ensure that we are comparing the same angular scales at both frequencies, we specified that the same minimum baseline length was used in producing the final images at both wavelengths. The largest angular size to which the images

are sensitive is approximately  $23''$ . We then smoothed the  $\lambda = 20 \text{ cm}$  image to a resolution of  $9''.52 \times 7''.65$  in order to match the resolution of the 90 cm observations.

Second, there could be a positional offset between the observing wavelengths. Though the  $\lambda = 90 \text{ cm}$  field of view contains many isolated point sources, none of these are within the  $\lambda = 20 \text{ cm}$  field of view. Slightly south of 3C 10, there is a moderately resolved source, B0022+637. This source was aligned on our two images. As a further check for any offsets across our images, we examined the  $\alpha_t = -0.46$  tomography map (§ 3) because this map best represents the spectral index of the source as a whole and should therefore have the lowest rms. We produced a series of these tomography maps in which the  $\lambda = 90 \text{ cm}$  image was shifted in right ascension and declination, and we determined the shift that produced the lowest rms. Using this criterion, the  $\lambda = 90 \text{ cm}$  image was shifted by  $-0''.764$  in right ascension and by  $-1''.209$  in declination. Note that this is a conservative procedure in that it tends to *reduce* any spectral variations.

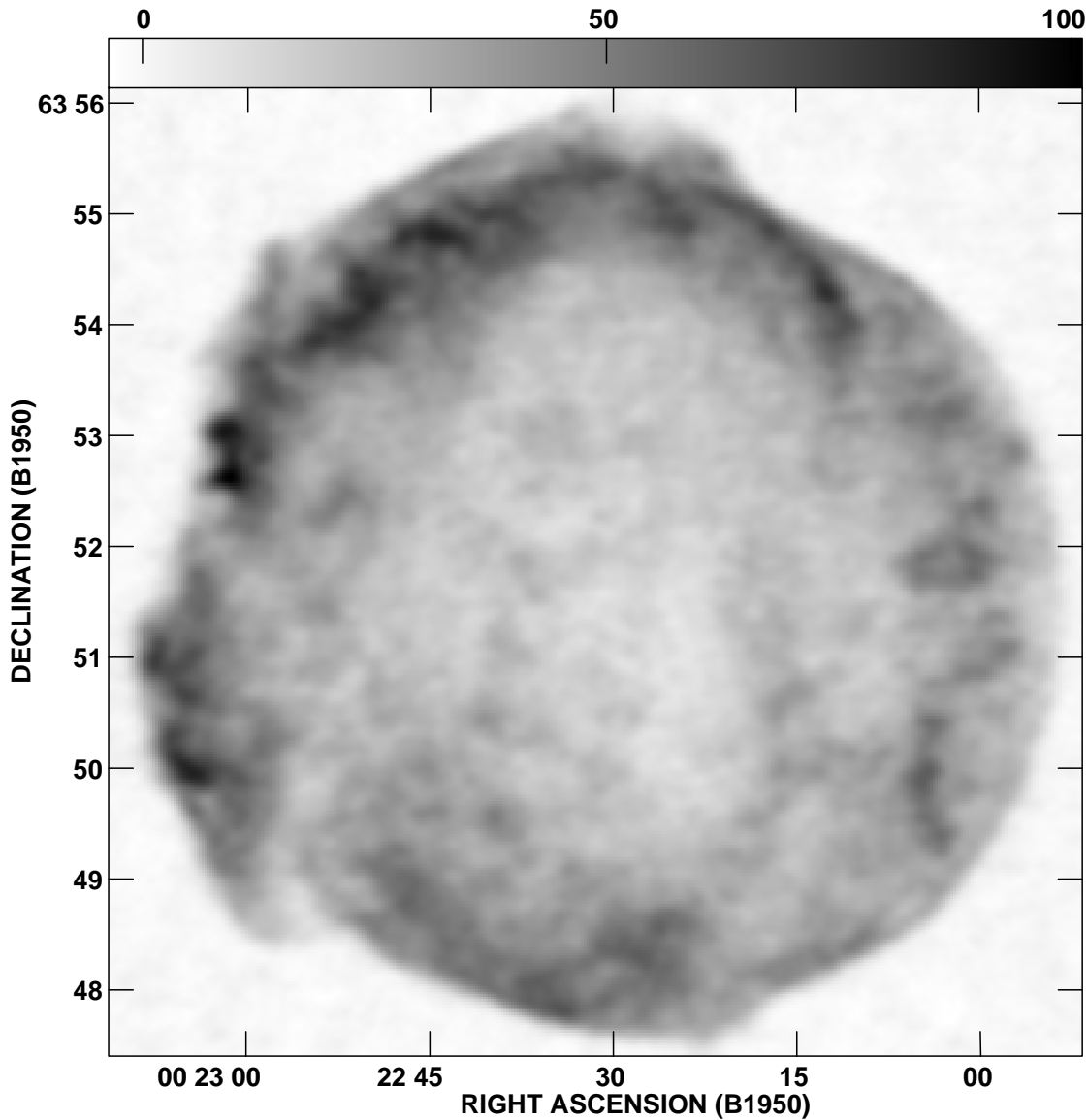


FIG. 2.—3C 10 at 90 cm. Gray-scale levels are linear between  $-3.8$  and  $101 \text{ mJy beam}^{-1}$ . The beam is  $9''.52 \times 7''.65$ , and the off-source noise level is  $0.9 \text{ mJy beam}^{-1}$ .

Third, the 20 and 90 cm data were acquired at different times, and the 90 cm data were themselves acquired over an interval of almost 2 yr. In that time, 3C 10 expanded on average by approximately 0.2%. Similar to our procedure above, we produced a series of  $\alpha_t = -0.46$  tomography maps in which the 90 cm image was expanded uniformly by small amounts. An expansion of 0.263% produced the smallest rms in this tomography map and is therefore the expansion that we adopted.<sup>3</sup> Again, this procedure tends to *reduce* any spectral variations. However, as Reynoso et al. (1997) found, Tycho is not expanding symmetrically. In order to test for any effects of asymmetric expansion on our spectral index determinations, we considered separately each of the five sectors Reynoso et al. (1997) identified as having a relatively uniform expansion. For each sector we tested four different amounts by which that sector had expanded between the epochs of the 20 cm and 90 cm obser-

vations: no expansion, 0.113%, 0.263%, and 1%. For each sector-expansion amount combination, we compared the flux density and spectral index in annuli as a function of distance from the center of the remnant. We took the center of the remnant to be the expansion center identified by Reynoso et al. (1997). Even an unlikely expansion of 1% would change our results marginally for the outermost regions of the source. We found that our results below are insensitive to any further corrections for expansion.

Finally, using the aligned images, we checked for a possible flux density calibration bias by plotting the 90 cm data against the 20 cm data. An extrapolation back to zero flux density at one wavelength should correspond to zero flux density at the other wavelength, otherwise there exists a zero-point offset (e.g., Katz-Stone, Rudnick, & Anderson 1993). We found a  $+0.5 \text{ mJy beam}^{-1}$  offset for which we corrected. However, in addition to this global offset, there appear to be additional offsets ranging from a few to as high as  $8 \text{ mJy beam}^{-1}$  in the inner  $100''$  of the remnant. We are unable to make further corrections, and, as discussed below,

<sup>3</sup> A bias can occur when the spectral indexes are determined *visually*, but the rms is then insensitive to this bias.

this will make interpretation of our results in these regions ambiguous.

Both of our images (Figs. 1 and 2) show a number of similar characteristics:

1. A limb-brightened shell structure;
2. Brightness enhancements along the northern and eastern rims; and
3. Several filaments of enhanced brightness in the interior of the remnant (Fig. 3).

The interior filaments tend to be elongated along the north-south axis. These filaments were originally identified in the tomography gallery as explained below, but a careful inspection of the total intensity images also reveals these filaments.

### 3. SPECTRAL INDEX OF 3C 10

Our objective is to search for variations in the shape of the radio synchrotron spectrum across 3C 10. The presumption is that changes in the shape of the spectrum signal changes either in the strength of the acceleration process or in the acceleration process itself, either currently or earlier in the evolution of the blast wave. We begin by determining

the spectral index as a function of distance from the center of the remnant. We then search for finer-scale variations in the spectral index, using the technique of spectral tomography (Katz-Stone 1995; Katz-Stone & Rudnick 1997a, 1997b).

Figures 4, 5, 6, 7, and 8 show the flux density at  $\lambda = 20$  cm and  $\lambda = 90$  cm as a function of distance from the expansion center for each of the five sectors identified by Reynoso et al. (1997). Each point was derived by integrating the brightness at  $\lambda = 20$  cm and  $\lambda = 90$  cm over a  $10''$  annulus. The uncertainties are the off-source noise level reduced by the square root of the number of independent points (i.e., the number of beams) in each annulus. At 90 cm, these figures show a bright limb component that peaks between approximately 55 and 70 mJy and one or two inner components that peak between 20 and 40 mJy. At 20 cm the sectors show the same general features, though at lower flux density levels. In general, the spectral indexes are constant within the errors, except for a slight tendency for regions of lower flux density tend to have flatter spectral indexes. However, since the lower surface brightness regions are in the inner part of the source, where we have found evidence for an additional offset between the two wavelengths (§ 2), we cannot con-

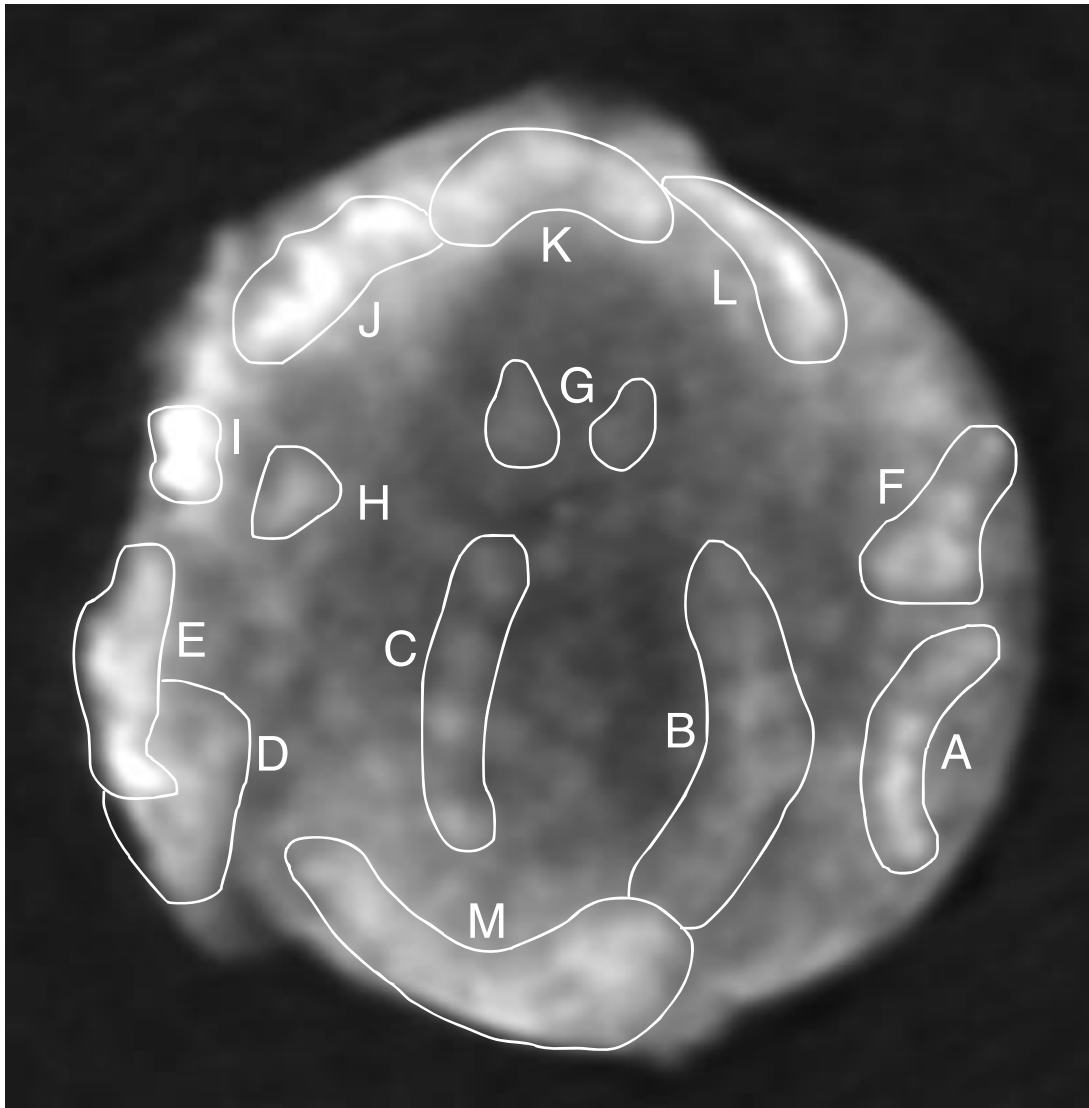


FIG. 3.—Filaments identified in the interior of 3C 10. Their locations are shown on the total intensity 20 cm image (Fig. 1).

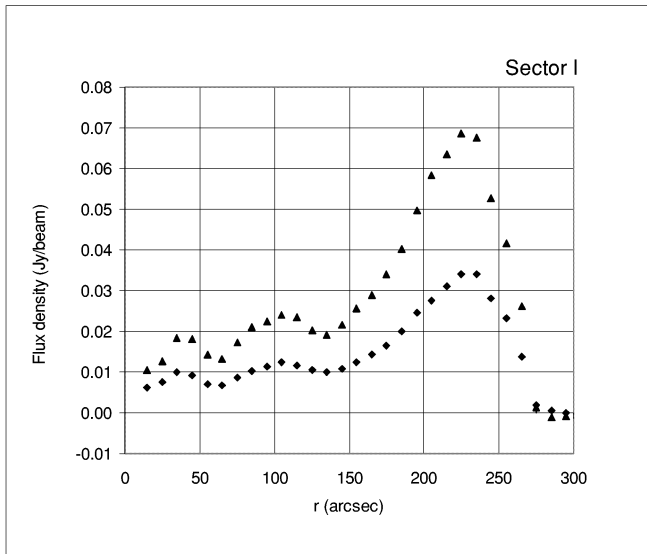


FIG. 4.—Flux density as a function of distance from the center of 3C 10 within sector I. Triangles show the flux density at 90 cm, and diamonds show the flux density at 20 cm. The flux densities were determined by integrating the brightness over a  $10''$  annulus. This sector was identified by Reynoso et al. (1997) as having a relatively uniform expansion rate.

clude that there are any significant spectral variations in the central  $100''$  of the remnant.

Figures 4–8 are sufficient to show the gross structure of the flux density distribution within the remnant. However, the interferometric data have a much higher angular resolution, and finer-scale structure—should it exist—could be detected. In order to probe for fine-scale spectral index changes inside the remnant, we have used a spectral tomography method.

Spectral tomography involves making a gallery of tomography maps in which each tomography map is

$$I_t(\alpha_t) \equiv I_{90} - \left( \frac{v_{90}}{v_{20}} \right)^{\alpha_t} I_{20}, \quad (1)$$

where  $I_{90,20}$  are the images at 20 and 90 cm. Regions that disappear from the tomographic image  $I_t$  with  $\alpha_t$  have a

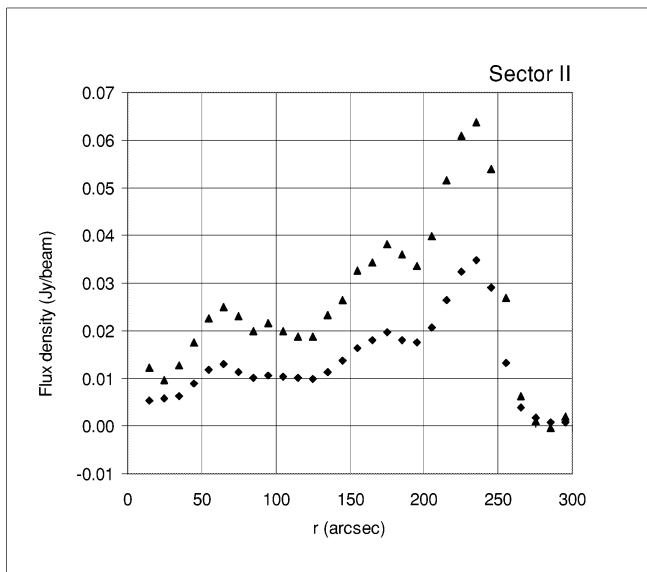


FIG. 5.—Same as Fig. 4, but for sector II

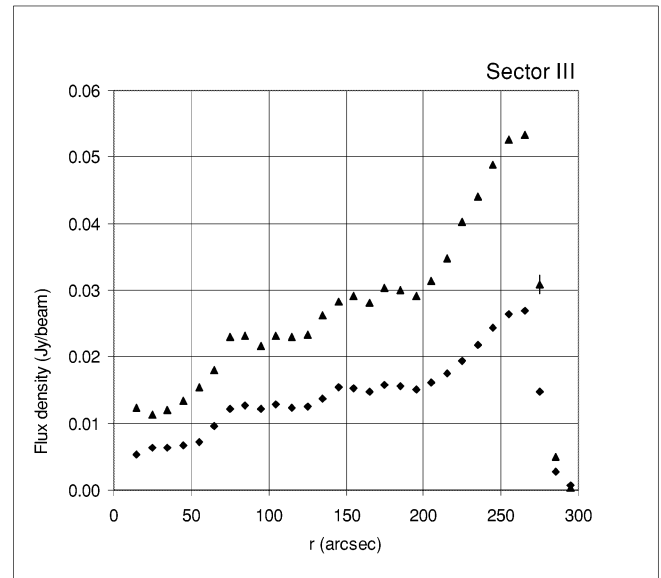


FIG. 6.—Same as Fig. 4, but for sector III

spectral index  $\alpha_{90}^{20} = \alpha_t$  (Katz-Stone 1995; Katz-Stone & Rudnick 1997a, 1997b).<sup>4</sup>

The tomography map  $I_t$  can be used to determine (overlapping) regions having differing spectral indexes. However, the spectral indexes so determined can be biased by any (remaining) flux density offset between images at the two wavelengths. In order to avoid a bias in our determination of the spectral indexes, we used a  $\chi^2$  minimization technique. We define the  $\chi^2$  as

$$\chi^2(\alpha_t) \equiv \sum \left[ \frac{I_t(\alpha_t) - \langle I_t(\alpha_t) \rangle}{\sigma_t} \right]^2. \quad (2)$$

Here,  $\sigma_t(i, j)$  is the off-source rms noise level propagated through to the tomography map,  $\langle I_t(\alpha_t) \rangle$  is the average over a small region in the tomography maps, and the sum is over pixels in that region.

<sup>4</sup> Our gallery of tomographic maps, in an MPEG movie format, is available on-line at <http://rsd-www.nrl.navy.mil/7213/lazio/Tycho/>.

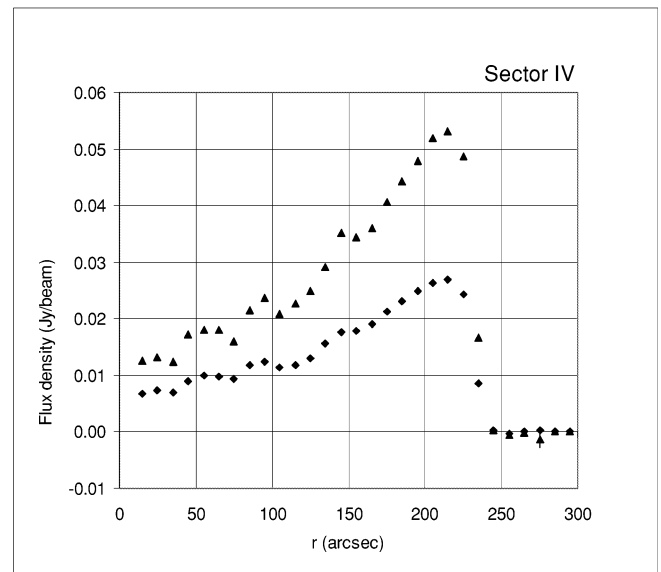


FIG. 7.—Same as Fig. 4, but for sector IV

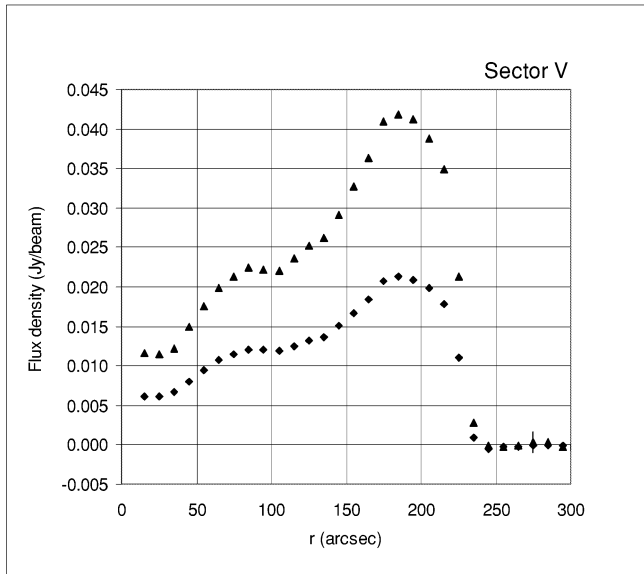


FIG. 8.—Same as Fig. 4, but for sector V

Using spectral tomography, we have identified 13 bright, filamentary features and five relatively filament-free (“background”) regions. Figure 3 shows the 13 bright features’ locations on a total intensity image, and Tables 3 and 4 tabulate relevant parameters for the filaments and “background” regions, respectively. The spectral indexes in Tables 3 and 4 were determined by finding the tomography

map that minimized the  $\chi^2$  for that region. The errors represent the  $1\sigma$  confidence of that minimization. In addition to the spectral index of each filament, we have determined its central position,  $\lambda = 20$  cm flux density, and distance from the center of the remnant. We took the central point for each filament to be its midpoint in each direction. We take the distance from the center of the remnant to be the straight-line distance between the remnant’s center and the filament’s center. Isolating the filaments’ flux density from the background component proved difficult. We attempted Gaussian fits for slices across the filaments, but there are too many parameters to provide a reliable fit. Instead we averaged the brightness at 20 cm in the regions indicated in Figure 3. This clearly overestimates the flux density, the implications of which we will discuss below.

Although the individual regions are quite distinct, the average spectral index between the background regions and filaments is the same. The spectral index for the background regions of the source has an average value of  $\langle\alpha\rangle = -0.52 \pm 0.02$ , while that of the filaments is  $\langle\alpha\rangle = -0.500 \pm 0.007$ . These average values were determined by finding the map that minimized  $\chi^2$  for all of the background regions or filaments simultaneously.

The filaments themselves show a general trend of increasing flux density with distance from the center, but no overall change in spectral index with either flux density or distance from the remnant’s center (Figs. 9, 10, and 11). Assuming that the background component has a flat or decreasing brightness profile, then any contamination in our determination of a filament’s flux density by the background com-

TABLE 3  
FILAMENTS WITHIN 3C 10

Filament	R.A.	Decl.	$S$ (mJy)	Spectral Index ( $\alpha_{90}^{20}$ )	Offset (arcmin)
A .....	00 22 18.61	63 50 27.1	25.2	$-0.50 \pm 0.03$	3.3
B .....	00 22 24.39	63 50 01.9	14.7	$-0.51 \pm 0.03$	2.4
C .....	00 22 34.47	63 50 43.9	14.5	$-0.44 \pm 0.03$	1.3
D .....	00 22 44.09	63 49 40.9	21.6	$-0.57 \pm 0.02$	3.9
E .....	00 22 45.77	63 50 56.5	28.5	$-0.51 \pm 0.02$	3.8
F .....	00 22 17.95	63 52 03.7	23.2	$-0.54 \pm 0.05$	3.3
G .....	00 22 30.83	63 53 02.5	11.9	$-0.6 \pm 0.1$	1.3
H .....	00 22 40.35	63 52 23.3	20.6	$-0.46 \pm 0.07$	2.4
I .....	00 22 44.65	63 52 48.5	39.4	$-0.44 \pm 0.02$	3.6
J .....	00 22 38.58	63 54 29.3	32.6	$-0.63 \pm 0.06$	3.4
K .....	00 22 30.93	63 55 23.9	28.0	$-0.55 \pm 0.02$	3.7
L .....	00 22 23.55	63 54 34.9	29.8	$-0.48 \pm 0.02$	3.4
M .....	00 22 35.59	63 48 26.7	26.0	$-0.53 \pm 0.02$	3.5

NOTES.—The average flux density  $\langle S \rangle$  of the filaments is at 20 cm. The filament’s offset is measured from 00<sup>h</sup>22<sup>m</sup>30<sup>s</sup>.926 and 63° 51′ 44″.110. Units of right ascension are hours, minutes, and seconds, and units of declination are degrees, arcminutes, and arcseconds.

TABLE 4  
BACKGROUND REGIONS WITHIN 3C 10

Feature	R.A.	Decl.	Size (arcsec)	Spectral Index ( $\alpha_{90}^{20}$ )
NE .....	00 22 41.18	63 53 02.1	54.6 × 58.8	$-0.55 \pm 0.04$
SE .....	00 22 47.50	63 51 25.7	28.0 × 41.0	$-0.45 \pm 0.08$
SW .....	00 22 08.84	63 51 20.1	26.6 × 35.0	$-0.40 \pm 0.15$
NW .....	00 22 19.82	63 53 10.5	47.6 × 51.8	$-0.72 \pm 0.14$
Center .....	00 22 28.49	63 50 03.4	84.0 × 121.8	$-0.52 \pm 0.02$

NOTE.—Units of right ascension are hours, minutes, and seconds, and units of declination are degrees, arcminutes, and arcseconds.

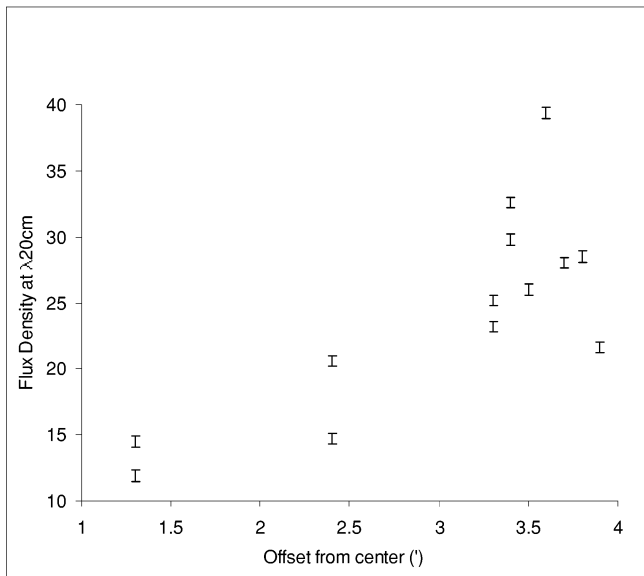


FIG. 9.—Filament distance from the center of 3C 10 as a function of its flux density at 20 cm.

ponent would become less severe with increasing distance. In these cases, the general trend between flux density and distance may actually be stronger.

While the full set of filaments does not show a correlation between spectral index and flux density, those filaments in the outer ring (A, D, E, F, I, J, K, L, and M, shown as filled squares in Fig. 11) do show a significant correlation: correlation coefficient of 0.81 with a significance level of 99%. Figure 11 shows that, for these outer filaments, brighter filaments tend to have a flatter spectral index. However, this trend is highly dependent upon filament I, which is the brightest and flattest spectral index filament.

To summarize our results, we have found that (1) a number of regions with somewhat different spectral indexes, “filaments,” exist within 3C 10; (2) the average spectral index of the filaments and the background component is

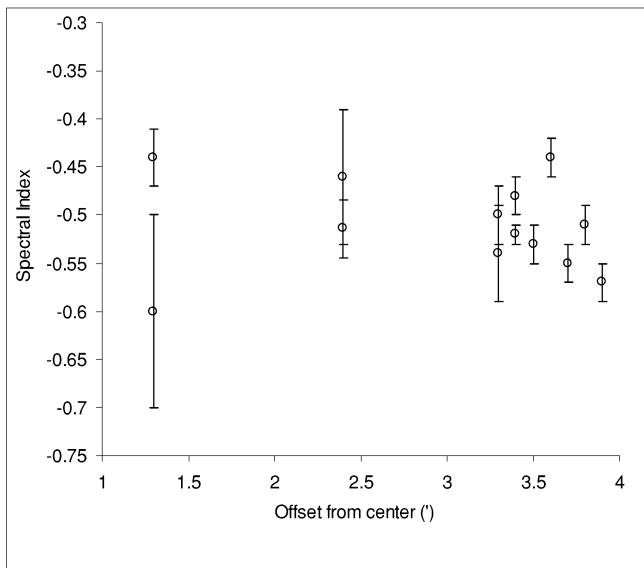


FIG. 10.—Filament spectral index as a function of distance from the center of 3C 10.

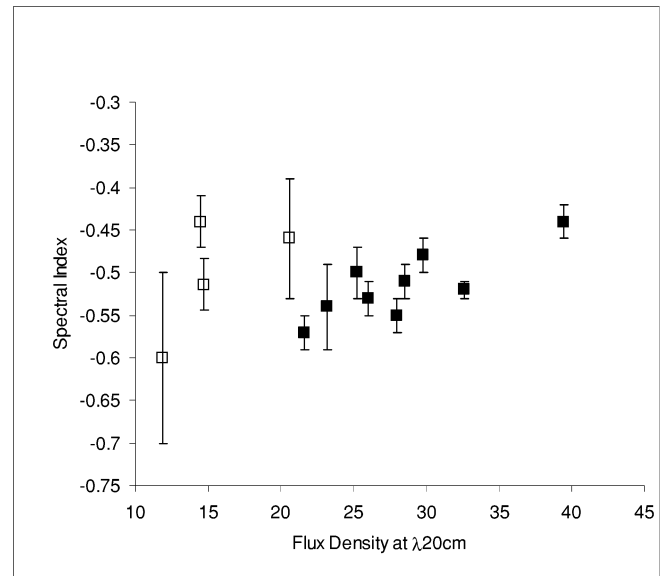


FIG. 11.—Filament spectral index as a function of 20 cm flux density. Filled squares represent the outer filaments (A, D, E, F, I, J, K, L, and M), as explained in the text.

consistent; (3) the brightest filaments tend to be in the outer region of 3C 10; (4) in general, the spectral indexes of the filaments do not show a trend with flux density or position; and (5) however, the spectral indexes of filaments in the outer rim do show a correlation such that bright filaments tend to have flatter spectral indexes.

#### 4. DISCUSSION

In general our results support the role of first-order Fermi acceleration in Tycho. The first-order Fermi mechanism for a strong shock predicts a spectral index of  $-0.5$  (Bell 1978; Eilek & Hughes 1991), which is consistent with our average results for both the background component and the filaments. Further, for Mach numbers greater than approximately 5, the spectral index should not vary by more than about 0.1 (e.g., Blandford & Eichler 1987), which is also consistent with our results.

Previous observations of the synchrotron spectrum of 3C 10 have not reached a consensus on whether spatial variations exist in the spectral index (Kundu & Velusamy 1971; Roger et al. 1973; Duin & Strom 1975; Klein et al. 1979; Vinyaikin et al. 1987). Indeed, one of the motivations for conducting the 90 cm observations with the VLA was to obtain higher resolution images to address the question of spectral index variations within the remnant. Using spectral tomography, we have found that a number of distinct regions with different spectral indexes, “filaments,” can be identified within 3C 10. Close inspection of a high-resolution,  $\lambda = 6$  cm image presented by Duin & Strom (1975) reveals that a number of these filaments, filaments E, I, J, L, M, and possibly B, were detected, though those authors did not mention them explicitly.

In addition, we find that the brighter filaments are in the outer regions and may have a slight trend with spectral index such that brighter filaments have flatter spectral indexes; this is epitomized by the brightest and flattest spectral index filament, filament I. These trends may help to determine details of the acceleration mechanisms. However,



with images at only two frequencies, we can only suggest various hypotheses that could explain the existence of the filaments and the trends we have detected. These hypotheses divide naturally into two categories: SNR blast wave–ambient medium interactions or internal inhomogeneities of the magnetic field within the SNR.

Collisions between the SNR blast wave and the interstellar medium will both increase the flux density and flatten the spectrum if the shock begins to become radiative locally (Jones et al. 1998). This mechanism would tend to produce filaments more efficiently in the outer regions of the remnant, thereby explaining the trend of increasing flux density with increasing distance from the remnant's center. That the filaments are most numerous in the outer portions of the remnant is modest support for this possibility.

It is also suggestive that there are more filaments on the eastern edge of 3C 10 than on the western edge. The eastern side of 3C 10 is expanding more slowly than the western side (Reynoso et al. 1997), an asymmetry that Reynoso et al. (1999) attribute to high-density H I found only on the eastern edge of the remnant. Further, the flattest-spectrum filament (filament I) is in sector II of Reynoso et al. (1997)—the most slowly expanding sector. The interaction between the expanding blast wave and a high-density ambient medium would generate radiative shocks with stronger postcompression shock densities and magnetic field strengths. Powerful support for this hypothesis that filaments indicate radiative shocks is the detection of optical emission from filament I by Kamper & van den Bergh (1978).

An alternate scenario for the observed spectral variations within 3C 10, involving internal inhomogeneities, is a curved electron energy spectrum observed in various magnetic field strengths. A detailed analysis of SNR HB 9 has shown that this is a reasonable scenario for the outer regions of that remnant (Leahy et al. 1998). If the electron energy spectrum hardens at lower frequencies (“concave-down”), regions in which the magnetic field is higher than the surroundings will both appear brighter and have a flatter spectrum than the surroundings. A concave-down spectrum is consistent with the Galactic synchrotron background, which breaks around 100 MHz (Longair 1994 and references therein), or may be due to locally accelerated electrons with a curved energy spectrum. In either case, regions in which the magnetic field is stronger would appear both brighter and with a flatter spectrum.

There is some evidence that the magnetic field is stronger in the outer region of Tycho. Heavens (1984)—who presented a Sedov solution for particle acceleration in 3C 10—argued that the extremely limb-brightened radio images must be explained by variations in the magnetic field, specifically, a limb that is dominated by filaments having a higher magnetic field. While this suggestion is intriguing, to determine whether the flat spectrum we see for the brightest filament (filament I) is due to a curved synchrotron spectrum in a strong magnetic field, we would need a solid estimate of the magnetic field throughout the SNR and the shape of the spectrum.

With observations at two frequencies, we cannot determine whether the synchrotron spectrum has the requisite concave-down (curved) shape. However, there is some ambiguous evidence that *counters* this scenario.

The integrated spectrum between 10 and 2000 MHz appears to be concave-up (Braude et al. 1970; Roger et al.

1973). The integrated spectrum peaks at 18 MHz and hardens above a few hundred MHz. Roger et al. (1973) were able to model the spectrum with two components—a flat component with  $\alpha = -0.35$  and a steep component with  $\alpha = -0.95$ . Reynolds & Ellison (1992) used a nonlinear shock calculation of first-order Fermi acceleration to generate model synchrotron spectra. They find excellent agreement with the integrated spectrum of 3C 10 if the synchrotron spectrum is concave-up. In contrast, Vinyaikin et al. (1987) find that the integrated spectrum in this same frequency range is a power law with a single spectral index  $\alpha = -0.61 \pm 0.03$ . Further high-resolution, high-dynamic range observations at three well-spaced frequencies would be useful in clarifying the shape of the spectrum at each position in the source (Katz-Stone et al. 1993).

As a final note, recent observations and analysis of the SNR Cas A have been interpreted with spatial variations in the spectral index being due to power laws of different slopes rather than a single curved spectrum (Wright et al. 1999). These authors concluded that the strength of particle acceleration varies across Cas A. Without a conclusive determination of the shape of the synchrotron spectrum, we cannot eliminate this possibility in 3C 10.

Most of this discussion has focused upon the moderate correlation between spectral index and flux density that is seen in the outer filaments (primarily filament I). The total set of filaments does not show this sort of correlation. For example, filaments B and C have nearly the same flux density, but different spectral indexes (Fig. 11). This is similar to the results Anderson & Rudnick (1993) found for “younger” remnants. They concluded that two unrelated mechanisms are responsible for the spectral index and flux density. While the spectral variations we report here are small, our conclusion is similar to Anderson & Rudnick (1993).

## 5. CONCLUSION

We have carried out a sensitive, high-resolution, radio spectral index study of 3C 10 (Tycho's SNR) between 20 and 90 cm. Previous spectral index studies of supernova remnants in general, and this remnant in particular, have been limited by the poor image fidelity and angular resolution of the low-frequency images. We have used a polyhedral-faceting imaging algorithm to produce a thermal-noise-limited  $\lambda = 90$  cm image of 3C 10, thereby improving significantly the accuracy and precision of the spectral indexes we derive.

We find localized spatial variations in the continuum spectrum that must be explained in context of the acceleration process responsible for generating the synchrotron-emitting relativistic electrons. In particular, we find that filaments in the outer regions of 3C 10 show a trend between flux density and spectral index.

With images at only two frequencies, we cannot distinguish between various mechanisms that might produce the trend we observe in these filaments. Competing mechanisms include SNR blast wave–ambient medium interaction and internal inhomogeneities of the magnetic field within the remnant. On the eastern edge of the remnant, the filaments are most numerous—suggesting regions where the blast wave is interacting with the cooler, clumped, preexisting structures in the circumstellar or general interstellar medium environment of the progenitor star. Some support for this scenario is provided by the detection of optical

emission from the brightest filament, filament I, indicating that it may be a radiative shock. Alternatively, a single electron energy spectrum can explain the observations if it hardens at lower frequencies (i.e., its shape is concave-down) and if the brighter filaments have higher magnetic field strengths.

Of course, some combination of these two mechanisms might also be operative. For instance, the filaments might trace radiative shocks at the blast wave–ambient medium boundary—with naturally higher compression ratios, densities, and magnetic field strengths—which themselves are immersed in a curved electron energy spectrum.

A high-fidelity image made at a third frequency could test the hypothesis of an underlying curved electron spectrum. The new 74 MHz ( $\lambda = 4$  m) system at the VLA is now capable of providing subarcminute-resolution, high-sensitivity (less than 25 mJy) images of supernova remnants including 3C 10. Furthermore, simultaneous 90 cm data are

obtained (Kassim et al. 1993), allowing compensation for any time variations within the remnant. Concurrent  $\lambda = 18$  cm or  $\lambda = 20$  cm VLA observations could then be used to test the curved electron spectrum hypothesis.

We thank D. Moffett and R. Perley for providing the data from their observations of 3C 10. We thank L. Rudnick (our referee), M. Brenner, D. Edsall, C. Schneider, A. Whiting, and S. Reynolds for productive discussions. We thank J. Imamura for assistance with the figures. The Very Large Array is a facility of the National Radio Astronomy Observatory, operated by Associated Universities, Inc., under contract with the National Science Foundation. This research was supported, in part, by the Naval Academy Research Council and Office of Naval Research grant N0001498WR20010. T. J. W. L. was supported an NRL–National Research Council Associateship. Basic research in radio astronomy at the NRL is supported by the ONR.

#### REFERENCES

- Anderson, M. C., & Rudnick, L. 1993, *ApJ*, 408, 514  
 Bell, A. R. 1978, *MNRAS*, 182, 147  
 Blandford, R., & Eichler, D. 1987, *Phys. Rev.*, 154, 1  
 Brahe, T. 1573, *De Nova Stella* (Copenhagen: Laurentius)  
 Braude, S. Y., Megn, A. V., Ryabov, B. P., & Zhouck, I. N. 1970, *Ap&SS*, 8, 275  
 Cornwell, T. J., & Perley, R. A. 1992, *A&A*, 261, 353  
 Duin, R. M., & Strom, R. G. 1975, *A&A*, 39, 33  
 Eilek, J. A., & Hughes, P. A. 1991, in *Beams and Jets in Astrophysics*, ed. P. Hughes (Cambridge: Cambridge Univ. Press), 428  
 Heavens, A. F. 1984, *MNRAS*, 211, 195  
 Hwang, U., & Gotthelf, E. V. 1997, *ApJ*, 475, 665  
 Jones, T. W., et al. 1998, *PASP*, 110, 125  
 Kamper, K. W., & van den Bergh, S. 1978, *ApJ*, 224, 851  
 Kassim, N. E., Perley, R. A., Erickson, W. C., & Dwarakanath, K. S. 1993, *AJ*, 106, 2218  
 Katz-Stone, D. M. 1995, Ph.D. thesis, Univ. Minnesota  
 Katz-Stone, D. M., & Rudnick, L. 1997a, *ApJ*, 479, 258  
 ———. 1997b, *ApJ*, 488, 146  
 Katz-Stone, D. M., Rudnick, L., & Anderson, M. C. 1993, *ApJ*, 407, 549  
 Keohane, J. W., Petre, R., Gotthelf, E. V., Ozaki, M., & Koyama, K. 1997, *ApJ*, 484, 350  
 Klein, U., Emerson, D. T., Haslam, C. G. T., & Salter, C. J. 1979, *A&A*, 76, 120  
 Koyama, K., Petre, R., Gotthelf, E. V., Hwang, U., Matsura, M., Ozaki, M., & Holt, S. S. 1995, *Nature*, 378, 255  
 Kundu, M. R., & Velusamy, T. 1971, *ApJ*, 163, 231  
 Leahy, D. A., Xizhen, Z., Xinji, W., & Jiale, L. 1998, *ApJ*, 339, 601  
 Longair, M. S. 1994, *High Energy Astrophysics*, Vol. 2 (Cambridge: Cambridge Univ. Press)  
 Lozinskaya, T. A. 1992, *Supernovae and Stellar Winds in the Interstellar Medium* (New York: AIP)  
 Reynolds, S. P., & Ellison, D. C. 1992, *ApJ*, 399, L75  
 Reynoso, E. M., Moffett, D. A., Goss, W. M., Dubner, G. M., Dickel, J. R., Reynolds, S. P., & Giacani, E. B. 1997, *ApJ*, 491, 816  
 Reynoso, E. M., Velázquez, P. F., Dubner, G. M., & Goss, W. M. 1999, *AJ*, 117, 1827  
 Roger, R. S., Bridle, A. H., & Costain, C. H. 1973, *AJ*, 78, 1030  
 Strom, R. G., Goss, W. M., & Shaver, P. A. 1982, *MNRAS*, 200, 473  
 Tan, S. M., & Gull, S. F. 1985, *MNRAS*, 216, 949  
 Tanimori, T., et al. 1998, *ApJ*, 497, L25  
 Vinyai, E. N., Volodin, Y. V., Dagkesamanskii, R. D., & Sokolov, K. P. 1987, *Soviet Astron.*, 21, 141  
 Wright, M., Dickel, J., Koralesky, B., & Rudnick, L. 1999, *ApJ*, 518, 284